Multiple scattering and nonlinear thermal emission of Yb^{3+}, Er^{3+}:Y_2O_3 nanopowders

S. Redmond and S. C. Rand[a)]
Department of Electrical Engineering and Computer Science, University of Michigan, Ann Arbor, Michigan 48109

X. L. Ruan and M. Kaviany
Department of Mechanical Engineering, University of Michigan, Ann Arbor, Michigan 48109

(Received 2 September 2003; accepted 15 January 2004)

Radiation transport and multiple scattering calculations are presented and compared with experimental observations to characterize light attenuation in high emissivity nanopowders irradiated with low power laser light at room temperature, and to explain the associated white light emission and the onset of melting. Using radiation tuned to an absorption resonance of Yb^{3+} dopants in Y_2O_3 nanopowder, we observed the onset of intense blackbody emission above a well-defined intensity threshold. Local melting of the compact above threshold leads to the formation of single crystal microtubes. Evidence is provided to show that two-flux transport theory and diffusion theory both significantly underestimate the absorption due to dependent, multiple scattering and that the threshold for the thermal runaway process responsible for this behavior is very sensitive to porosity of the random medium. © *2004 American Institute of Physics.*
[DOI: 10.1063/1.1667274]

I. INTRODUCTION

Properties of porous random nanomedia can be quite different from those of uniform solids of the same composition. In recent years it has been confirmed that the microscopic details of porous networks strongly affect their thermal conductivity,[1] local fields,[2] and radiative lifetimes of luminescent impurities both through changes in effective dielectric constant[3] and quantum size effects.[4] It has also been shown that electrically pumped, continuous-wave laser action can be sustained in nanoscale regions of rare-earth-doped nanopowders without any apparent cavity.[5,6] Here we present evidence that other aspects of thermal and optical transport in highly porous, ultrafine nanopowders are dramatically different from those of homogeneous solids.

In this article, unexpectedly efficient laser heating of high emissivity oxide powders doped with trivalent rare-earth ions is reported. As a function of incident optical intensity, under steady-state conditions, luminescent emission from the powder sample is shown to undergo a sequence of stages involving the appearance of upconversion,[7,8] its subsequent quenching and eventual reappearance of emission in the form of a broadband visible continuum. These interactions are decidedly unexpected, in view of the high sample reflectivity which makes it difficult for light to penetrate and elicit any response at all. It has previously been shown[9] that the luminescence quenching and continuum emission in Yb^{3+}, Er^{3+}:Y_2O_3 nanopowders result from a nonlinear heating process involving principally the Yb ion, but no detailed balance arguments have been presented to analyze the initiation of thermal emission in high albedo samples using transport theory. Prior work elsewhere also revealed broad spectral emission upon laser irradiation of silicon nanopowders.[10] However, here we present results for dielectric nanopowders that permit a detailed comparison with the Planck blackbody spectrum over a wide range of wavelengths and leaves no doubt as to the origin of the observed continuum emission in dielectric nanopowders. They also reveal the importance of sample porosity in facilitating the effect. We carefully explore the roles of strong scattering and heat transport at nanopowder surfaces to understand how runaway heating is initiated and sustained on surfaces of very high albedo. We also consider whether ''dependent'' scattering (multiple scattering with coherent field addition) or light localization play any significant role in these unusual laser-matter interactions.

The structure of the article is as follows. In Sec. II we step through a sequence of theoretical models based on (i) independent scattering, (ii) a first-order correction to independent scattering for coherent contributions, and (iii) a two-flux radiation transport theory, respectively. This helps establish what aspects of electromagnetic propagation are necessary to predict heating and melting of high emissivity powders by low intensity radiation. In Sec. III we then describe experimental procedures that were used to create and study the nonlinear luminescence conditions of interest here. Experimental results are presented in Sec. IV and discussed in Sec. V.

By comparing theory and experiment, the role played by local variations of nanopowder reflectivity (over distances on the order of the wavelength) in elevating scattering rates and increasing local absorption and heating is examined. Attenuation lengths predicted by even the most comprehensive (two-flux) model are found not to be in quantitative agree-

a)Author to whom correspondence should be addressed; electronic mail: scr@eecs.umich.edu

ment with pure scattering measurements at wavelengths far from the Yb resonance. On resonance, the experimental extinction length shows even poorer agreement with predictions, pointing out the serious inadequacy of transport theory of absorption when strong, dependent scattering is present in highly porous media. The onset of melting is shown theoretically to depend strongly on the effective thermal conductivity, reflectivity and porosity of the sample, and melting is predicted only at locations with high porosities ($0.4<\varepsilon<0.9$), at the power levels of our experiments.

II. THEORY

The attenuation due to scattering in a random nanomedium is predicted first for independent scattering and then by including dependent scattering approximately to account for spatial correlations of the fields scattered by close-packed spherical particles. Dependent scattering is multiple scattering in which coherent field addition occurs and correlations among scattering waves are important. It arises when scattering events take place within a distance shorter than the spatial period of the electromagnetic wave of frequency ω. This requires that near fields from adjacent scatterers overlap,[11] a condition that enormously complicates theoretical analysis. In nanopowders, when the particle density is on the order of 100 per cubic wavelength, this complication is unfortunately unavoidable. Dependent scattering calculations can be performed exactly for one-dimensional layered dielectrics,[12] accounting completely for coherent addition of fields and attendant properties in the high density limit. Of importance for the discussion here is the finding that light is increasingly transmitted through random media as particles less than a wavelength in size are brought close together, despite the reduction of the scattering mean free path to subwavelength values. This may not seem unexpected since, as porosity goes to zero, one rapidly approaches the limit of fully dense, nonabsorbing solids that are transparent in the effective medium limit. In recent experiments though[12] it has been reported that even at 15% of full density a similar regime may be found in which the mean free path is shorter than the wavelength and yet transparency becomes relatively high in three-dimensional scattering media. Here we provide evidence that traditional transport theory is inadequate to explain attenuation lengths on the order of millimeters at visible wavelengths in porous samples with mean free transport distances that are less than an optical wavelength.

Attenuation distances for scattering and absorption are first predicted using several approaches based on Mie theory. Then, using the most comprehensive approach to radiative transfer, the two-flux approximation, energy balance is explored within the model of laser-matter interaction depicted in Fig. 1. This is the basis for applying radiation transport theory to predict melting dynamics under the conditions of our experiments.

A. Attenuation

We begin by calculating attenuation length in a system of independent scatterers. We assume the porosity of the random medium is high and nonuniform, with a significant distribution in particle sizes, in order to simulate closely the conditions of our experiments.

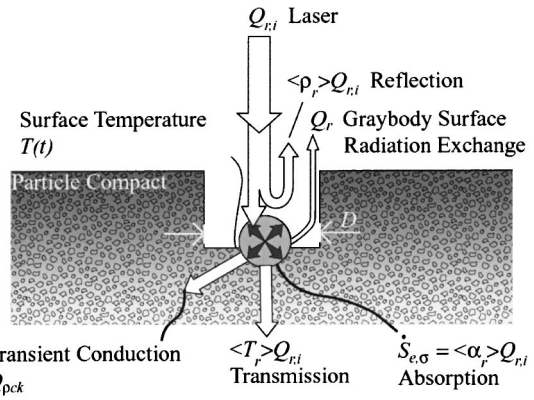

FIG. 1. Schematic diagram of the transport model of thermal and radiative balance at the sample surface. Irradiation, reflection, absorption, and conduction processes are taken into account.

A scanning electron micrograph (SEM) of a yttria nanopowder surface is shown in Fig. 2. The average particle size in the photo is 30 nm, too small to be seen on the same scale as the micron-sized, empty pore regions in as-grown material. This photo illustrates the variability of porosity on the scale of the optical wavelength. In some regions there are clusters of particles, whereas other regions are empty, showing that the local porosity can be much higher or lower than the average. The average porosity $\langle\varepsilon\rangle$ in the SEM appears to be 0.5, but is actually much higher due to the porous nature of particle clusters on the nanometer scale. So the powders are neither uniformly dense nor monodisperse, and were taken in our calculations to have a mean diameter $\langle d_p\rangle$ and a rectangular distribution of particle size ($\pm\Delta d_p$).

For small particles, with size parameters $\alpha=\pi d_p/\lambda\ll 1$ satisfying the Rayleigh limit, the scattering and absorption efficiencies are given by[1]

$$\eta_s=\frac{8}{3}\alpha^4\left|\frac{\varepsilon_e-1}{\varepsilon_e+1}\right|^2, \tag{1}$$

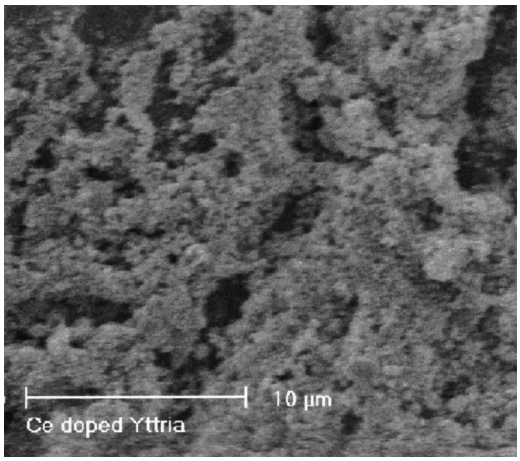

FIG. 2. Micrograph of doped yttria powder compact. Regions of high porosity are evident.

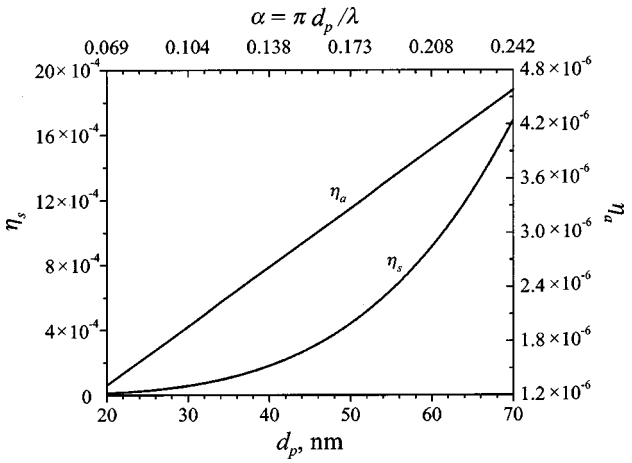

FIG. 3. Efficiencies η_s and η_a for independent scattering and absorption of single, spherical particles, calculated using the Rayleigh and Mie theories, as a function of particle diameter for $\lambda=906$ nm, $n_s=1.8$, and $\kappa_s=1.2\times10^{-5}$.

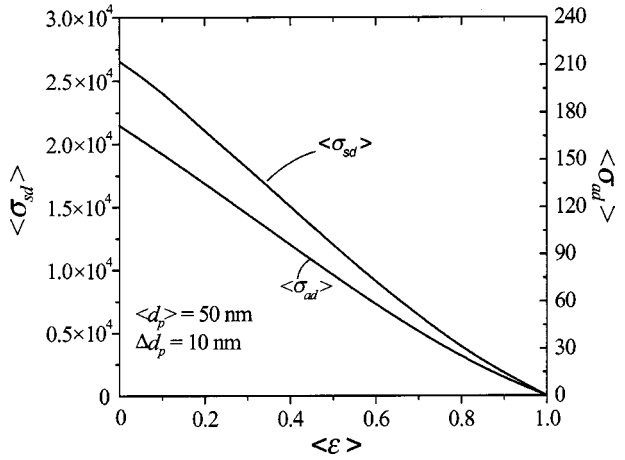

FIG. 4. Variation of predicted effective, dependent scattering and absorption coefficients with respect to the effective porosity for $\lambda=906$ nm, $n_s=1.8$, and $\kappa_s=1.2\times10^{-5}$.

$$\eta_a = 4\alpha\,\mathrm{Im}\left(\frac{\varepsilon_e-1}{\varepsilon_e+1}\right), \tag{2}$$

where ε_e is the relative dielectric constant, $\varepsilon_e=(n_s+i\kappa_s)^2$. Note that in dielectric samples such as ours, κ_s arises strictly from bound electron response (atomic absorption) and does not give rise to surface wave and plasmonic effects that can produce spectral modifications in the near-field region in systems with conduction electrons. For larger particles, Mie theory is used, and since the analytic expressions are cumbersome, a computer program UNO can be used to calculate the efficiencies.[13] Figure 3 shows the variation of the η_s and η_a calculated in this way for yttria particles of various sizes. For convenience, Rayleigh theory was used for η_s and η_a at an excitation wavelength of $\lambda_{ex}=906$ nm, and particle sizes were assumed to be in the range 20–70 nm.

Next, to include the dependent scattering and absorption at an effective porosity of 0.85, we examined a typical first-order approach developed for small particles in Ref. 14. The authors in Ref. 14 allowed for electromagnetic field interference outside the particles, to obtain a two-parameter correction to correlations among scattered fields. Their correction makes reasonable predictions for very small size parameters, but gives negative scattering efficiency for large particles. Here we use a simpler correction, which gives predictions similar to those in Ref. 14 for small particles, while avoiding its deficiency for large particles. Correcting for dependent scattering, we have[1]

$$\eta_{sd}=\eta_s[1+1.5(1-\langle\varepsilon\rangle)-0.75(1-\langle\varepsilon\rangle)^2], \tag{3}$$

$$\eta_{ad}=\eta_a[1+1.5(1-\langle\varepsilon\rangle)-0.75(1-\langle\varepsilon\rangle)^2]. \tag{4}$$

Using these expressions and accounting for the particle size distribution $N(d_p)\Delta d_p$ that specifies the number of particles with diameter between d_p and $d_p+\Delta d_p$ per unit volume, the effective spectral scattering and absorption coefficients are found to be[1]

$$\langle\sigma_{sd}\rangle=\int_{d_{p1}}^{d_{p2}}\eta_{sd}(d_p)\,\frac{\pi d_p^2}{4}N(d_p)\,dd_p, \tag{5}$$

$$\langle\sigma_{ad}\rangle=\int_{d_{p1}}^{d_{p2}}\eta_{ad}(d_p)\,\frac{\pi d_p^2}{4}N(d_p)\,dd_p. \tag{6}$$

To evaluate Eqs. (5) and (6), we assumed a uniform distribution of diameters in the range $\langle d_p\rangle\pm\Delta d_p$, so that $d_{p1}=\langle d_p\rangle-\Delta d_p$, $d_{p2}=\langle d_p\rangle+\Delta d_p$, and the number density $N(d_p)$ was taken to be

$$N(d_p)=\frac{1-\langle\varepsilon\rangle}{\int_{d_{p1}}^{d_{p2}}\frac{\pi d_p^3}{6}\,\mathrm{d}d_p}=\frac{24(1-\langle\varepsilon\rangle)}{\pi(d_{p2}^4-d_{p1}^4)}. \tag{7}$$

Equations (3), (4), (5), (6), and (7) were then used to determine $\langle\sigma_{sd}\rangle$ and $\langle\sigma_{ad}\rangle$ versus effective porosity $\langle\varepsilon\rangle$. The predicted results are shown in Fig. 4.

Using these results, we now turn to the solution of the equation of radiative transfer (ERT) containing the effective scattering and absorption coefficients. As an effective medium treatment, ERT is not capable of completely capturing the dependent scattering effects. For that purpose, Maxwell's equations, with boundary conditions at all the particle-pore interfaces, should be solved. This sort of calculation has been done for one-dimensional layered dielectrics,[12,15] and the results show a field enhancement phenomenon due to constructive interference of the scattered fields. This enhancement is thought to exist also in randomly packed, poly-sized spherical particles,[16] however direct simulations in three dimensions are too cumbersome to be practical at the present time. It was suggested in Ref. 15 that the results of ERT are statistically equivalent to the average of the direct simulations (after introducing corrections to the scattering and absorption efficiencies based on the dependent scattering). Thus, we use this approach here, with the corrections of radiative properties given by Eqs. (3) and (4), to predict the intensity distribution through the medium.

Assuming semi-isotropic intensities I^+ and I^-, the equations of the two-flux model are[17]

$$\frac{dI^+}{dx}=-(\overline{\sigma}+\overline{a})I^+ +\overline{\sigma}I^-, \tag{8}$$

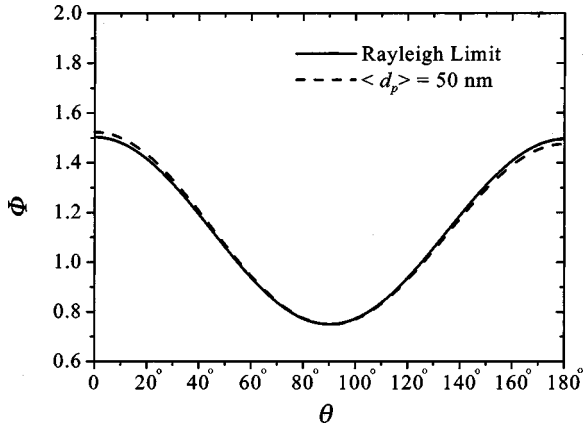

FIG. 5. Variation of independent scattering phase function predicted from Rayleigh (solid) and Mie (dashed) theory, with respect to the polar angle for $\lambda=906$ nm, $n_s=1.8$, and $\kappa_s=1.2\times10^{-5}$.

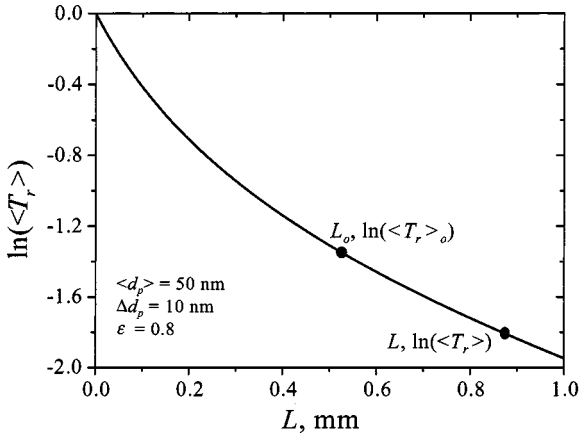

FIG. 6. Variation of effective transmission with respect to sample thickness calculated for $\lambda=906$ nm, $n_s=1.8$, and $\kappa_s=1.2\times10^{-5}$.

$$-\frac{dI^-}{dx}=-(\overline{\sigma}+\overline{a})I^-+\overline{\sigma}I^+, \tag{9}$$

where $\overline{a}=2\langle\sigma_{ad}\rangle$, $\overline{\sigma}=2B\langle\sigma_{sd}\rangle$, and $B=1/2\int_{-1}^{0}\Phi(\theta)d\cos\theta$ is the backscatter fraction. Blackbody emission is neglected in this attenuation analysis, although it has recently been shown that the near-field effects of emission may be very important in nanoscale radiative transfer.[18,19] For media that support resonant surface waves, the radiative energy exchange can be enhanced by several orders of magnitude between a blackbody radiator and a test particle, and must be taken into account.[20] However, such near-field effects are not important in lossless dielectrics that cannot excite plasmonic surface waves. Additionally, the complete neglect of the far-field emission in the attenuation analysis is justified in the next section, where the contribution of the emitted energy is shown to be very small, compared to the scattering and absorption.

The predicted distribution of the scattering phase function is shown in Fig. 5, for particles near the Rayleigh regime. Both Rayleigh and Mie results are shown in the figure, however. Near the Rayleigh limit, the scattering is semi-isotropic and the phase function $\Phi(\theta)=3/4(1+\cos^2\theta)$ yields a backscattering fraction of $B=0.5$. For 50 nm particles the Rayleigh and Mie results are similar. For larger particles, scattering is stronger in the forward direction and Mie scattering theory should be used.

The boundary conditions for Eqs. (8) and (9) are $I^+(0)=1$ and $I^-(L)=0$; these equations may be solved for the effective transmittance $\langle T_r\rangle$ and reflectance $\langle\rho_r\rangle$. The results are

$$\langle T_r\rangle=I^+(L)=\frac{2\beta}{(1+\beta^2)\sinh(\gamma L)+2\beta\cosh(\gamma L)}, \tag{10}$$

$$\langle\rho_r\rangle=I^-(0)=\frac{(1-\beta^2)\sinh(\gamma L)}{(1+\beta^2)\sinh(\gamma L)+2\beta\cosh(\gamma L)}, \tag{11}$$

where

$$\beta=[\overline{a}/(\overline{a}+2\overline{\sigma})]^{1/2},\quad \gamma=[\overline{a}(\overline{a}+2\overline{\sigma})]^{1/2}. \tag{12}$$

In Eq. (10), $\langle T_r\rangle$ is a function of sample thickness L, and the variation of $\ln\langle T_r\rangle$ with respect to L is shown in Fig. 6. For small L the initial variation of $\ln\langle T_r\rangle$ is nonlinear, but for large L it becomes linear asymptotically. This is due to the $2\beta\cosh(\gamma L)$ term in Eq. (10), which vanishes for large L. By defining an attenuation length ℓ_{att} according to

$$\frac{\langle T_r\rangle}{\langle T_r\rangle_0}=\exp\left(-\frac{L-L_0}{\ell_{att}}\right), \tag{13}$$

the asymptotic slopes of plots like Fig. 6 can be used to compare attenuation in thick random dielectric media using the expression

$$\ell_{att}^{-1}=-\frac{\ln(\langle T_r\rangle)-\ln(\langle T_r\rangle_0)}{L-L_0}. \tag{14}$$

The attenuation lengths predicted from the two-flux model for various particle sizes are discussed further in Sec. V.

The two-flux model presented above is an important extension of earlier diffusive wave models[21] that now includes dependent scattering to first order. In Eqs. (8) and (9), the last term on the right of each equation represents a contribution to the propagating flux coming from re-scattering of radiation previously scattered in the backward direction. These terms introduce independent and dependent multiple scattering in such a way that no assumption is made about the incident plane wave becoming directionally randomized after propagating a certain distance (z_p in Ref. 21). This latter approach leads to an internal source term and different boundary conditions compared to the two-flux model but does not make the particle size dependence explicit. The adequacy of the present model is compared directly with that of Ref. 21 in the discussion.

B. Melting

In this section a simple transient thermal analysis is used to predict the time of onset of melting t_m. Because of strong scattering the incident field is exponentially attenuated, causing absorption (proportional to the square of the field) to take place mainly in a thin layer very near the surface of the medium. For simplicity, it is therefore assumed in our melting analysis that absorption takes place right at the surface.

This allows for an analytic solution to the transient conduction. We also treat the radiative emission as a surface emission for the same reason (as will be shown, due to the dominance of thermal conduction, this emission is negligible). The amount of energy absorbed is determined from the two-flux model. The predicted melting onset time is to be considered a lower limit (compared to that expected from a distributed energy treatment).

Figure 1 provides a schematic diagram of the irradiation, absorption, and transmission of light through the powder, as well as the formation of a molten well in the material. Upon wicking and evaporation, this well deepens to form a cylindrical hole in the compact. At the surface of the compact, the surface energy equation is[22]

$$Q_{\rho ck}+Q_r=\dot{S}_{e,\sigma}, \tag{15}$$

where

$$\dot{S}_{e,\sigma}=\langle\alpha_r\rangle Q_{r,i}, \tag{16}$$

$$Q_{\rho ck}=\frac{T(t)-T_\infty}{R_{\rho ck}(t)}. \tag{17}$$

Here $Q_{\rho ck}$, Q_r, and $Q_{r,i}$ specify energy flux rates for transient thermal conduction, net radiative exchange, and the incident radiation, respectively. The term $\langle\alpha_r\rangle$ is the absorbance and is given by $\langle\alpha_r\rangle=1-\langle\rho_r\rangle-\langle T_r\rangle$:$R_{\rho ck}$ is the conduction resistance and $\dot{S}_{e,\sigma}$ is the absorbed power, calculated from $Q_{r,i}$ by taking the absorbance into account.

The transient conductive heat transfer rate $Q_{\rho ck}$ varies over the circular area $x^2+y^2\leqslant(D/2)^2$ on the upper surface of the assumed, semi-infinite compact. Noting that the center of the circle ($x=0$, $y=0$) will have the highest temperature and largest conduction resistance, we select this point as the origin and take $Q_{\rho ck}$ to be constant. For the transient conduction resistance $R_{\rho ck}$ we find[23]

$$R_{\rho ck}=\frac{2(\langle\alpha\rangle t)^{1/2}}{\langle k\rangle}\left\{i\,\mathrm{erfc}(0)-i\,\mathrm{erfc}\left[\frac{D}{4(\langle\alpha\rangle t)^{1/2}}\right]\right\}, \tag{18}$$

where $\langle k\rangle$ and $\langle\alpha\rangle$ are the effective thermal conductivity and diffusivity, respectively, t is time, and $i\,\mathrm{erfc}$ is the complementary error function. The diameter $D=40\,\mu$m was selected to correspond with the experimental laser spot size. $\langle\alpha\rangle$ and $\langle k\rangle$ are related by the formula $\langle\alpha\rangle=\langle k\rangle/\langle\rho\rangle\langle c_p\rangle$, where $\langle c_p\rangle$ is the effective specific heat given by $\langle c_p\rangle=[(1-\langle\varepsilon\rangle)(\rho c_p)_s+\langle\varepsilon\rangle(\rho c_p)_f]/[(1-\langle\varepsilon\rangle)\rho_s+\langle\varepsilon\rangle\rho_f]$, and $\langle\rho\rangle$ is the effective density $\langle\rho\rangle=(1-\langle\varepsilon\rangle)\rho_s+\langle\varepsilon\rangle\rho_f$. The effective thermal conductivity is given by[1]

$$(\langle k\rangle/k_f)=(k_s/k_f)^{0.28-0.757\log(\varepsilon)-0.057\log(k_s/k_f)}. \tag{19}$$

Equation (19) shows that $\langle k\rangle$ decreases with increasing porosity ε. By virtue of Eq. (17), the conduction resistance therefore also increases with porosity. At $\langle\varepsilon\rangle=0.8$, the average values of the thermal conductivity, capacity, and diffusivity are $\langle k\rangle=0.094$ W/m K, $\langle c_p\rangle=502$ J/kg K, and $\langle\alpha\rangle=1.77\times10^{-7}$ m^2/s, based on solid and fluid densities of yttria $\rho_s=5046$ kg/m^3 and $\rho_f=1.177$ kg/m^3, respectively (yielding $\langle\rho\rangle=3280$ kg/m^3), thermal conductivities $k_s=15$ W/m K,[24] and $k_f=0.026$ W/m K, and thermal capacities $c_{p,s}=502.4$ J/kg K and $c_{p,f}=1005$ J/kg K.

The radiation heat flux Q_r is given by[22]

$$Q_r=\frac{\sigma_{\mathrm{SB}}[T(t)^4-T_\infty^4]}{R_{r,\varepsilon}+R_{r,F}+(R_{r,\varepsilon})_\infty}, \tag{20}$$

where

$$R_{r,\varepsilon}=\frac{1-\langle\varepsilon_r\rangle}{A_r\langle\varepsilon_r\rangle},\quad R_{r,F}=\frac{1}{A_rF},\quad (R_{r,\varepsilon})_\infty=0 \tag{21}$$

and σ_{SB} is the Stefan–Boltzmann constant, $\langle\varepsilon_r\rangle$ is the emissivity which is estimated as 0.5, A_r is the radiation surface, and F is the view factor. $T(t)$ is the temperature at time t. By substituting Eqs. (16)–(21) into Eq. (15), one finds

$$\frac{T(t)-T_\infty}{\frac{2(\langle\alpha\rangle t)^{1/2}}{\langle k\rangle}\left\{i\,\mathrm{erfc}(0)-i\,\mathrm{erfc}\left[\frac{D}{4(\langle\alpha\rangle t)^{1/2}}\right]\right\}}+\frac{\sigma_{\mathrm{SB}}[T(t)^4-T_\infty^4]}{\frac{1}{A_r\varepsilon_r}}=\langle\alpha_r\rangle Q_{r,i}. \tag{22}$$

For temperatures lower than the melting temperature T_m, sample radiation makes a negligible contribution to the overall energy balance. This can be seen on the basis of the comparative magnitudes of the two terms on the left side of Eq. (22).

$$\frac{T(t)-T_\infty}{\frac{2(\langle\alpha\rangle t)^{1/2}}{\langle k\rangle}\left\{i\,\mathrm{erfc}(0)-i\,\mathrm{erfc}\left[\frac{D}{4(\langle\alpha\rangle t)^{1/2}}\right]\right\}}\gg\frac{\sigma_{\mathrm{SB}}[T(t)^4-T_\infty^4]}{\frac{1}{A_r\varepsilon_r}}, \tag{23}$$

that is, to a very good approximation, Eq. (15) can be reduced to $Q_{\rho ck}=\dot{S}_{e,\sigma}$.

Implicit in Eq. (22) is the conclusion that the time to onset of melting t_m depends on the compact absorbance $\langle\alpha_r\rangle$. Upon close scrutiny of Eqs. (3), (4), (7), (9)–(11), we also find that $\langle\alpha_r\rangle$ is a function of porosity $\langle\varepsilon\rangle$. Figure 7 shows the dependence of $\langle\rho_r\rangle$, $\langle T_r\rangle$, $\langle\alpha_r\rangle$ on porosity explicitly. Note that $\langle\alpha_r\rangle$ decreases as $\langle\varepsilon\rangle$ increases. The variation in time to melt is shown in Fig. 8, for an incident power of $Q_{r,i}=400$ mW and a compact absorption of $\langle\alpha_r\rangle=0.04$. The results predict that melting occurs in less than 8 ms under these conditions. These equations also predict that t_m depends on the local porosity for a given irradiance. As discussed further in Sec. V, at low intensities Eq. (22) predicts no melting at any porosity for subthreshold intensities, then selective melting for porous regions at intermediate intensities, and finally complete melting at all porosities for very high intensity.

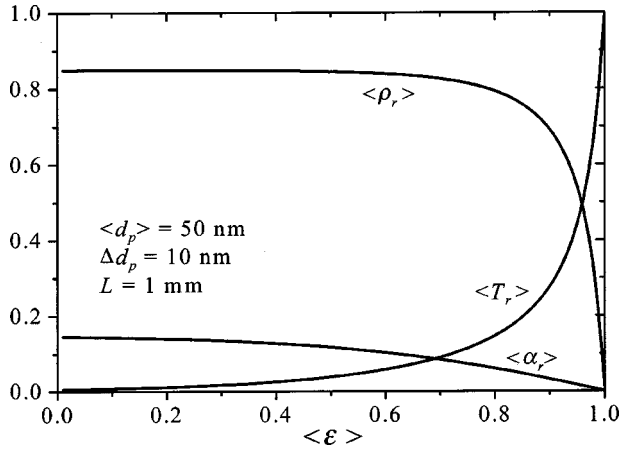

FIG. 7. Variation of compact effective reflectivity with respect to effective porosity of the compact, for a few values of sample thickness.

III. EXPERIMENTAL PROCEDURES

Samples for the present experiments were rare-earth-doped nanopowders (Yb^{3+},Er^{3+}:Y_2O_3) synthesized by flame spray pyrolysis as described in an earlier publication.[25] Particle size was 30 nm and compacts were prepared by lightly compressing powder into Al holders (at pressures <2 lb./in.^{2}) with a miniature press that achieved a filling fraction of approximately 0.15. The number of scatterers per wavelength in samples prepared this way greatly exceeded 1000 and scattering mean free paths were therefore much less than a wavelength. At such high densities dependent scattering should be prevalent. Consequently, we measured transmission properties and blackbody spectral dynamics in search of evidence that dependent scattering was necessary to account for our results.

The optical transmission through a free-standing nanopowder wedge was measured using an integrating sphere, with the sample placed at the entrance to the sphere. A continuous-wave Ti:sapphire laser was tuned to the wavelengths near the $^2F_{7/2}(0)\rightarrow{}^2F_{5/2}(2')$ resonance of Yb^{3+} at 905.6 nm, using a two-plate birefringent filter. The sample

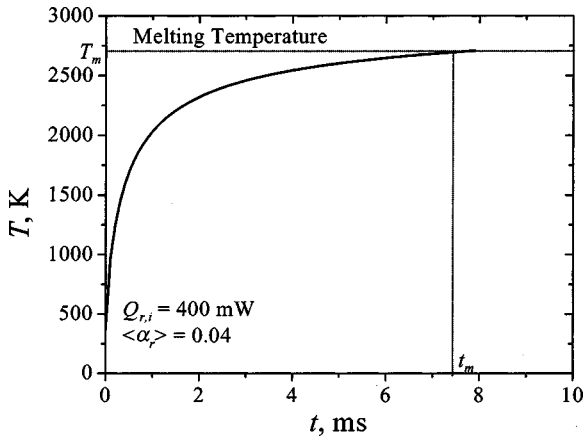

FIG. 8. Variation of peak surface temperature of the compact with respect to time, up to the onset of melting, calculated for an input power of 400 mW and $\langle\rho_r\rangle=0.78$. Other parameters were $\lambda=906$ nm, $n_s=1.8$, and $\kappa_s=1.2\times10^{-5}$.

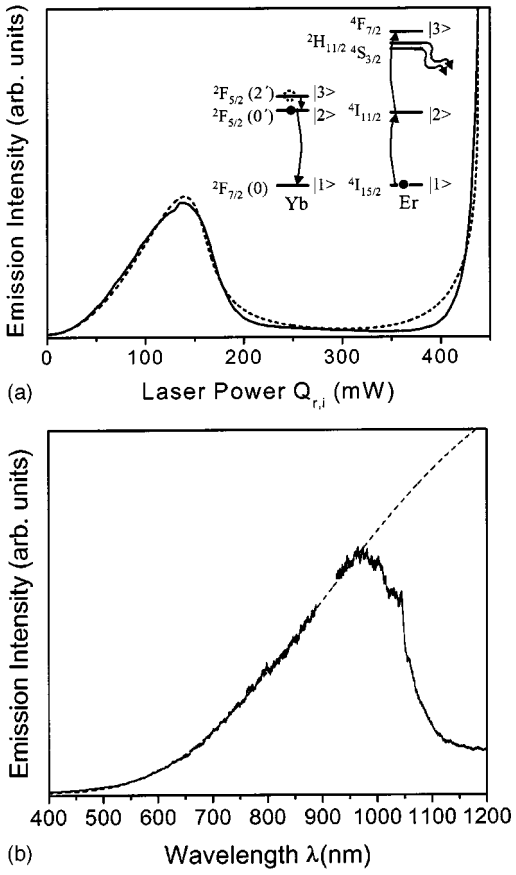

FIG. 9. (a) Luminescence intensity of Er, Yb:Y_2O_3 nanopowder as a function of input power, showing quenching of Er upconversion emission at powers just below 200 mW and the sudden onset of continuum radiation near 400 mW. Inset: schematic of energy transfer dynamics responsible for Er emission at low input powers. The laser is tuned to the resonant absorption of Yb^{3+} at $\lambda_{ex}=905.6$ nm, and the dashed curve gives the result of a detailed microscopic theory based on Eq. (15) of the present article and population rate equations as discussed in Ref. 9. (b) The spectrum of continuum emission, recorded with a 1 m spectrograph and photomultiplier with a cutoff wavelength of 960 nm (response corrected using a standard lamp calibration). The dashed curve is a fit to a Planck distribution with $T=1910$ K.

was translated parallel to the direction of increasing thickness, and the transmittance versus thickness was recorded with a photomultiplier. The attenuation lengths were then obtained for the wavelengths on and off the resonance. A more detailed account of these measurements has been published in Ref. 9. Sample emission versus incident intensity was also recorded on the erbium $^2H_{11/2}-{}^4I_{15/2}$ upconversion probe transition at $\lambda_{em}=522.4$ nm using a 1 m grating spectrometer. Full scans over the available range of intensities required 1/2 h or more. Results for total emission intensity versus excitation rate are given in Fig. 9(a). Similar results were obtained on all Yb and Er transitions, regardless of transition wavelength.

Samples irradiated with powers exceeding 400 mW exhibited very unusual emission characteristics. A bright white continuum appeared above an abrupt threshold of incident intensity. The spectrum of this emission was recorded with the spectrometer using a single grating and, after correction for instrumental response with a standard lamp, gave the result shown in Fig. 9(b). Samples subjected to intensities in

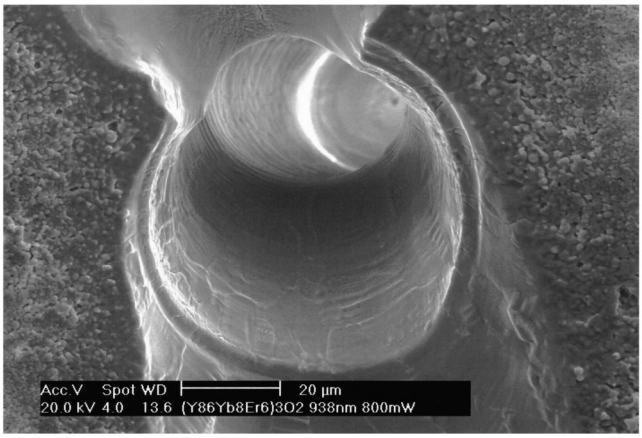

FIG. 10. Formation of hollow microtubes well above the white light threshold intensity.

excess of 30 kW/cm^2 were subsequently examined by scanning electron microscopy. They revealed clear evidence of melting (Fig. 10). Additionally, the formation of ceramic tubes was noted under these conditions and several were extracted for examination by sifting through irradiated powders.

IV. EXPERIMENTAL RESULTS

From our transmission measurements, characteristic lengths for experimental scattering lengths, total attenuation, and absorption were determined. The off-resonance attenuation length (due exclusively to elastic scattering at 870 nm) was found to be $\ell = 510\ \mu$m. The total attenuation length on resonance was 324 μm. Consequently, it was possible to determine the experimental absorption length for Yb^{3+} impurities in free-standing yttria powder from the difference of the inverse lengths to be $\ell_\alpha = 893\ \mu$m. These determinations permitted a direct comparison of the two-flux model prediction with experiment (See Sec. V).

Sample emission characteristics were found to vary dramatically with excitation rate in laser irradiation experiments. At low incident power luminescent intensity rose quadratically and was entirely due to rare-earth luminescence. In Fig. 9(a) this corresponds to the regime at the left of the figure below 100 mW. Behavior in this range was typical of Er luminescence sensitized by infrared-excited Yb impurities in yttria powders.[26,27] At higher input powers, luminescence underwent an abrupt and universal reversal, however. Luminescence was strongly quenched. Between 150 and 350 mW, all transitions steadily *decreased in intensity* [middle of Fig. 9(a)]. Next, above 350 mW in the figure, bright continuum emission appeared. This emission had the (instrumentally corrected) spectrum shown in Fig. 9(b). The dashed line shows the result of a fit to a Planck distribution with $T = 1910$ K. Excellent agreement is obtained with a blackbody curve at all wavelengths shorter than the detector cutoff at 960 nm. Data at the laser wavelength of 906 nm have been omitted because of the large Rayleigh peak there. Also, the apparent background at wavelengths longer than 1 μm is due to overlapping visible orders of the single grating used to perform the scan.

When the incident power was held at 350 mW and the sample position was scanned laterally, an interesting observation was made. White light was not generated uniformly over the sample surface. In only a few select locations was the nonlinear heating cycle effective enough at low input powers to reach the blackbody emission threshold on uniform, pristine surfaces. At significantly higher powers, white light could be generated at any location on the sample. Close physical and chemical examination of samples revealed no evidence of surface impurities that could catalyze such nonuniform response at low powers. Indeed flame spray pyrolysis yields as-grown powders with compositions virtually identical to the 99.99% pure precursor solutions. The powders are carbon free when proper oxidation conditions are maintained.[25] This indicated that some intrinsic property like local porosity of the surface was responsible for the variations.

At powers well over 400 mW, light-induced material processing occurred, as we noted earlier. The interior wall of one microtube that was formed from yttria nanopowder was later examined by small-angle electron diffraction. The results are presented in Figs. 11(a) and 11(b), respectively. Figure 11(a) shows the complete diffraction rings of a typical powder pattern. Figure 11(b), on the other hand, shows the re-solidified inner wall of the tube, exhibiting a fourfold symmetric pattern of spots consistent with cubic phase yttria. This pattern did not vary over distances of several hundred microns, further indicating that single crystal growth took place during the formation of the tube.

V. DISCUSSION

The measured attenuation lengths (off and on the absorption resonance) are compared in Fig. 12 with predictions of the two-flux model with ($\kappa_s = 1.2\times10^{-5}$) and without absorption ($\kappa_s = 0$), respectively. For values off resonance the attenuation differs from the calculation by only a factor of 2, whereas the measured extinction coefficient on resonance (including absorption) differs by considerably more from the theoretical prediction. This discrepancy may be due to a systematic error in the estimation of scattering coefficient κ_s, or it could be due to a breakdown of diffusion theory in the presence of strong dependent scattering. While specification of the particle size distribution (on the experiment side) or adequacy of the two-flux model (on the calculation side) are potential issues, independent results[12] suggest that this discrepancy is indeed a manifestation of the breakdown of diffusion theory and mean field approaches to multiple scattering in general.

From the results of Sec. II we can infer that regions with high local porosities melt most easily, and initiate melting in real compacts. Figure 13 shows the predicted time-to-melt t_m as a function of porosity, for various levels of irradiation between 200 and 500 mW. These results show that under conditions of high porosity ($0.4 \leqslant \langle \varepsilon_r \rangle \leqslant 1$) the compact melts in a fraction of a second at moderate powers, but that at low porosities it does not melt at all, regardless of incident power, on normal laboratory time scales. As the porosity decreases from 0.6 to 0.3 for $Q_{r,i} = 500$ mW, t_m increases by

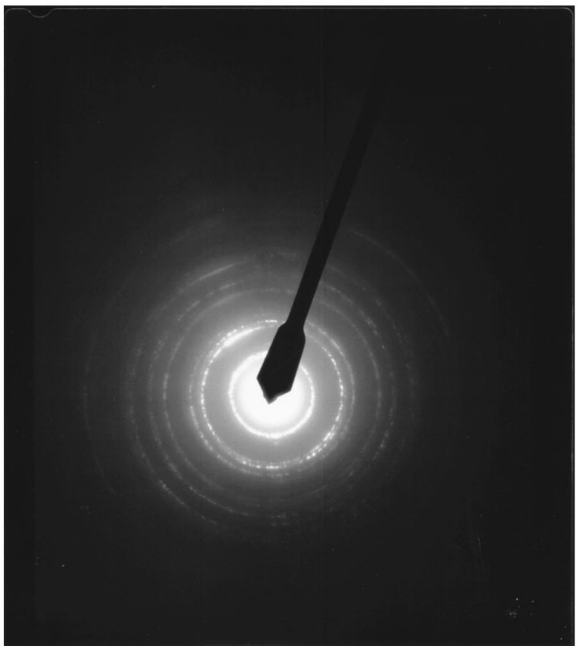

(a)

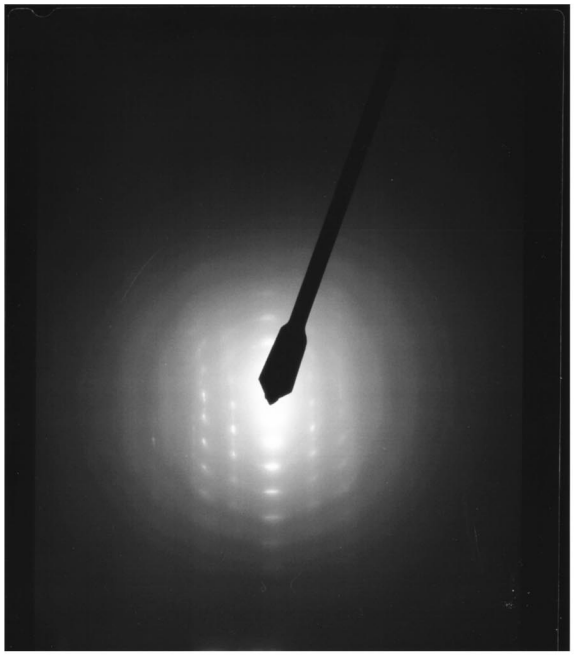

(b)

FIG. 11. Electron diffraction photos of (a) unprocessed powder and (b) the inner wall of a typical microtube.

nine orders of magnitude. Higher power levels do reduce the time to melt when the porosity is high enough to permit melting.

The main result of this analysis is that effective porosity plays a key role in determining whether melting takes place at a particular point on the sample surface. This agrees with the experimental observation that white light generation and melting vary markedly over the surface of a nominally ''uniform'' powder. Clearly *local porosity*, as sampled within the beam of the incident laser, is important in the initiation of resonant, nonlinear heating. So the inhomogeneous nature of the density distribution at the surface of our samples is an

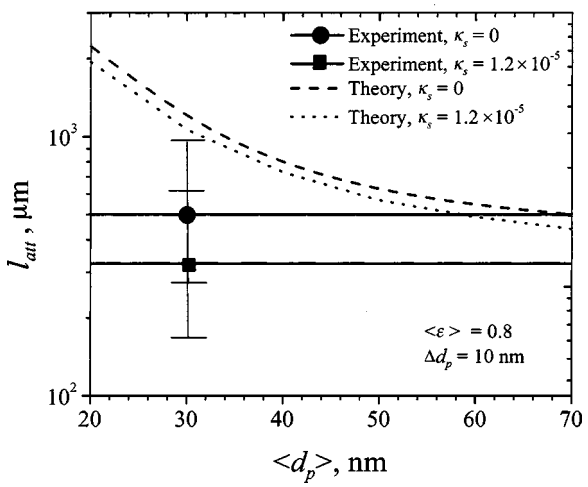

FIG. 12. Variation of predicted attenuation length with respect to average particle size, for several values of index of extinction at $\lambda=906$ nm and $n_s=1.8$. The experimental results on and off absorption resonance are also shown. The parameter is $\Delta d_p=10$ nm.

important contributing factor to thermal response in the light-surface interaction. Because dependent scattering is variable but pronounced at porosities as high as 0.9, it is possible that coherent multiple scattering plays an important role in the experimental results on initiation of melting and single crystal growth reported here. We have shown that transport theory cannot quantitatively predict the absorption length in our samples, so we are unable to show decisively that dependent scattering plays a dominant role in the phenomena described in this article. However, we cannot offer any mechanism other than dependent scattering to resolve the discrepancies. Improved models that account for dependent scattering effects without relying on ensemble averages or diffusion theory should be developed to improve the overall agreement with absorption, scattering, and light-induced melting behavior of dense multiple-scattering media.

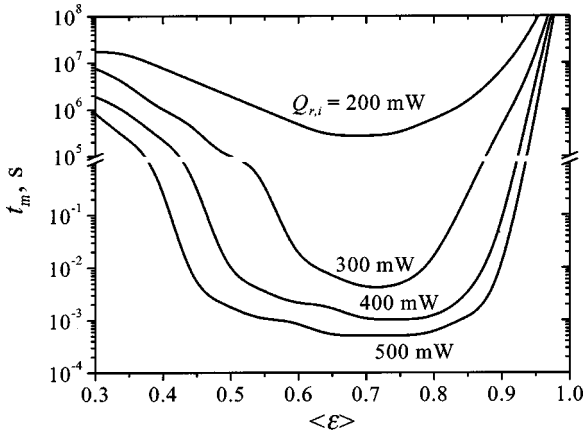

FIG. 13. Variation of the predicted times of the onset of melting, with respect to effective porosity $\langle\varepsilon\rangle$, for a few values of incident powers between 200 and 500 mW.

ACKNOWLEDGMENTS

The authors thank R. M. Laine, M. Kim, and J. Marchal for assistance with-sample characterization. This research was partially supported under AFOSR Grant No. F49620-03-1-0389.

[1] M. Kaviany, *Principles of Heat Transfer in Porous Media*, 2nd ed. (Springer, New York, 1995).
[2] A. K. Sarychev, V. A. Shubin, and V. M. Shalaev, Phys. Rev. B **60**, 16389 (1999).
[3] R. S. Meltzer, S. P. Feofilov, B. Tissue, and H. B. Yuan, Phys. Rev. B **60**, R14012 (1999).
[4] H. Schniepp and V. Sandoghdar, Phys. Rev. Lett. **89**, 257403 (2002).
[5] G. Williams, B. Bayram, S. C. Rand, T. Hinklin, and R. M. Laine, Phys. Rev. A **65**, 013807 (2001).
[6] B. Li, G. R. Williams, S. C. Rand, T. Hinklin, and R. M. Laine, Opt. Lett. **27**, 394 (2002).
[7] Y. Guyot, R. Moncorge, L. D. Merkle, A. Pinto, B. McIntosh, and H. Verdun, Opt. Mater. (Amsterdam, Neth.) **5**, 127 (1996).
[8] J. P. Wittke, I. Ladany, and P. N. Yocum, J. Appl. Phys. **43**, 595 (1972).
[9] S. M. Redmond, S. Oliveira, and S. C. Rand, Appl. Phys. Lett. (to be published).
[10] J. Costa, P. Roura, J. R. Morante, and E. Bertran, J. Appl. Phys. **83**, 7879 (1998).
[11] K. Kamiuto, J. Opt. Soc. Am. **73**, 1819 (1983).
[12] S. M. Redmond, S. L. Oliveira, G. L. Armstrong, H.-Y. Chan, M. Cui, E. Mattson, A. Mock, B. Li, J. R. Potts, S. C. Rand, J. Marchal, T. Hinklin, and R. M. Laine, J. Opt. Soc. Am. B **21**, 214 (2004).
[13] J. R. Mahan, *Radiation Heat Transfer* (Wiley, New York, 2002).
[14] S. Kumar and C. L. Tien, ASME J. Heat Transfer **112**, 178 (1990).
[15] X. L. Ruan and M. Kaviany, Proceedings of the 2003 ASME Summer Heat Transfer Conference, Las Vegas, NV, July 21–23, 2003.
[16] A. Nashashibi and K. Sarabandi, IEEE Antennas Propag. Mag. **47**, 1454 (1999).
[17] M. Q. Brewster and C. L. Tien, ASME J. Heat Transfer **104**, 573 (1982).
[18] A. V. Shchegrov, K. Joulain, R. Carminati, and J.-J. Greffet, Phys. Rev. Lett. **85**, 1548 (2000).
[19] R. Carminati and J.-J. Greffet, Phys. Rev. Lett. **82**, 1660 (1999).
[20] J.-P. Mulet, K. Joulain, R. Carminati, and J.-J. Greffet, Appl. Phys. Lett. **78**, 2931 (2001).
[21] N. Garcia, A. Z. Genack, and A. A. Lisyansky, Phys. Rev. B **46**, 14475 (1992).
[22] M. Kaviany, *Principles of Heat Transfer* (Wiley, New York, 2001).
[23] H. S. Carslaw and J. C. Jaeger, *Conduction of Heat in Solids* (Clarendon, Oxford, 1986).
[24] Y. S. Touloukian, R. W. Powell, C. Y. Ho, and P. G. Klemens, *Thermophysical Properties of matter*, Thermophysical Properties Research Center Data Series, Vol. 2 (IFI-Plenum, New York, 1970), pp. 240–241.
[25] R. M. Laine, T. Hinklin, G. Williams, and S. C. Rand, J. Metastable Nanocryst. Mater. (Switzer.) **8**, 500 (2000).
[26] F. Auzel, Proc. IEEE **61**, 758 (1973).
[27] S. M. Redmond and S. C. Rand, Opt. Lett. **28**, 173 (2003).